PHOTONICS Research

Transparently curved metamaterial with broadband millimeter wave absorption

Cheng Zhang,[1,†] Jin Yang,[1,†] Wenkang Cao,[1] Wei Yuan,[1] Junchen Ke,[1] Liuxi Yang,[1] Qiang Cheng,[1,2] and Tiejun Cui[1,3]

[1]State Key Laboratory of Millimeter Waves, Southeast University, Nanjing 210096, China
[2]e-mail: qiangcheng@seu.edu.cn
[3]e-mail: tjcui@seu.edu.cn

Received 2 November 2018; revised 30 January 2019; accepted 14 February 2019; posted 15 February 2019 (Doc. ID 350020); published 27 March 2019

We present a conformal metamaterial with simultaneous optical transparency and broadband millimeter-wave absorption for a curved surface. By tailoring the reflection response of meta-atoms at oblique angles, it is possible to achieve excellent absorption performance from 26.5 to 40.0 GHz within a wide angular range from 0° to 60° for transverse-electric and transverse-magnetic waves. In the meantime, by employing transparent substrates, including polyvinyl chloride and polyethylene terephthalate, good optical transmittance (80.1%) and flexibility are obtained simultaneously. The reflectivity of a curved metallic surface coated with the proposed curved metamaterial is simulated and measured experimentally. Both results demonstrate excellent absorption performance of the metamaterial, which is highly favored for practical applications.

https://doi.org/10.1364/PRJ.7.000478

1. INTRODUCTION

In the past few years, millimeter wave technology has become a new research hotspot for scientists and engineers; it is essential for many applications such as radar, imaging, and wireless communications. However, ubiquitous electromagnetic interferences and noises pose significant challenges to the quality of high-speed voice and data transmission. As important means of electromagnetic protection, millimeter-wave absorbers are widely employed to dissipate jamming signals, thereby greatly improving the overall performance of the systems [1,2]. A major drawback of traditional millimeter-wave absorbers [3–5] is low light transmittance, implying they cannot be applied as transparent shielding windows in some practical scenarios. In addition, due to the physical characteristics of the constituent materials, they are usually unable to offer enough flexibility in conformal applications with a low profile and a wide bandwidth.

As alternatives, metamaterials (MMs) [6,7] that can independently tailor electric and magnetic responses [8] have been proposed for resonant absorption, offering a new approach to realize conformal transparent millimeter-wave absorbers [9–11]. For instance, great efforts have been made to implement conformal metamaterial absorbers (MMAs) at terahertz and infrared spectra, but most of them suffer from the limitation of a narrow absorption bandwidth [12–18]. In addition, transparent-semiconductor-based broadband MMAs with large light transmittances have been developed at microwave frequencies, but lack of angular stability hinders their practical applications on curved surfaces [19–27].

To date, various approaches have been proposed to broaden the bandwidths of MMAs. An extremely wideband MMA based on destructive interference of the elements was built with multilayer structures containing split-ring resonators; it can induce successive anti-reflection in a large frequency range [28]. A comprehensive scheme based on the dispersion engineering of a spoof surface plasmon polariton was proposed to merge the absorption bands of a plasmonic structure into a continuous one [29]. In addition, by stacking metallic bars of varying lengths on three polyimide layers, a wide absorption spectrum in the THz region was formed by merging multiple successive resonances [30].

Here, we report a new strategy to design conformal and transparent MMAs, which can realize excellent absorption of millimeter waves over a Ka band from 26.5 to 40.0 GHz. A ring-shaped structure is employed as the basic element. It is a well-defined sandwich structure composed of indium tin oxide (ITO) patterns and transparent substrates including polyvinyl chloride (PVC) and polyethylene terephthalate (PET). Full-wave numerical simulations reveal that the absorption phenomenon originates from the resonant modes confined in the structure, with the resonances slightly influenced by the incident angle. It is found that for a curved metallic surface with an MMA coating, average radar cross-section (RCS) reduction of more than 10 dB is achieved within the bandwidth for both

transverse-electric (TE) and transverse-magnetic (TM) waves, as validated by simulation and experimental results. This work represents a significant step toward conformal transparent absorbers to suppress backward reflections from curved surfaces.

2. THEORY AND DESIGN

The schematic of the curved and transparent MMA is depicted in Fig. 1(a). A typical unit cell, illustrated in Fig. 1(b), consists of a ring resonator on the top PET film, a ground layer on the bottom PET film, and a PVC spacer as the substrate. Both the patterns and the ground are made of ITO film due to its good electrical conductivity. The top ITO layer has a thickness of 150 nm and a sheet resistance of 140 Ω/□, whereas the bottom ITO layer has a thickness of 200 nm and a sheet resistance of 15 Ω/□. All constituent materials employed in the proposed structure have outstanding flexibility and large optical transparency. The dielectric constants of PET and PVC are $\varepsilon_{\mathrm{PET}} = 3.0(1 - j0.006)$ and $\varepsilon_{\mathrm{PVC}} = 2.4(1 - j0.06)$, respectively. The dimensions of the unit cell in Fig. 1(b) are $d_{\mathrm{PET}} = 0.175$ mm, $d_{\mathrm{PVC}} = 1.3$ mm, $h = 1.65$ mm, $a = 4.8$ mm, $g = 0.7$ mm, and $P = 5.0$ mm.

The reason to choose a ring structure as the unit cell is twofold. On one hand, it is a classic meta-atom with simple geometry, a broad bandwidth, and satisfactory absorptivity [31,32]. On the other hand, owing to the symmetry of the element, the absorption performance is insensitive to the incidence polarization. To demonstrate these merits, Fig. 2(a) shows the simulated absorptivity spectra of the meta-atom under normal incidence based on a commercial electromagnetic solver (CST Microwave Studio 2014). It is noted that a broadband absorption band from 25.0 to 37.5 GHz (absorptivity > 0.9) emerges under normal illumination of a plane wave [Fig. 2(a)]. Such strong absorption originates from magnetic resonance driven by the incident wave, where antiparallel currents are induced between the pattern and the ground [Fig. 2(c)]. As a result, the excited magnetic fields are strongly concentrated between the currents [Fig. 2(b)], giving rise to a large energy dissipation by sheet resistance of the ring resonators. This makes a great difference from a conventional MMA, since the latter is based on the dielectric loss of the substrate in a narrow frequency band near the resonance of the metallic elements [33–36]. In contrast, the proposed element can operate in a wide bandwidth without the introduction of multi-resonances [37,38], since the lossy pattern will greatly lower the quality factor of the whole structure. In order to gain more physical insights into the absorption performance of the proposed MMA, the normalized input impedance of the absorber is also illustrated in Fig. 2(a), which is calculated from the S-parameters of the unit cell according to the effective medium theory [39,40]. It is clear that the impedance of the MMA [Fig. 2(a)] is well matched to that of free space in the spectrum of interest, resulting in satisfactory reduction of backward reflections at the interface.

Once the absorber is coated on a curved surface, it is important to inspect its absorption capability at oblique incidence, namely, the angular stability in the millimeter band. In fact, the equivalent transmission line (TL) model of the MMA can be

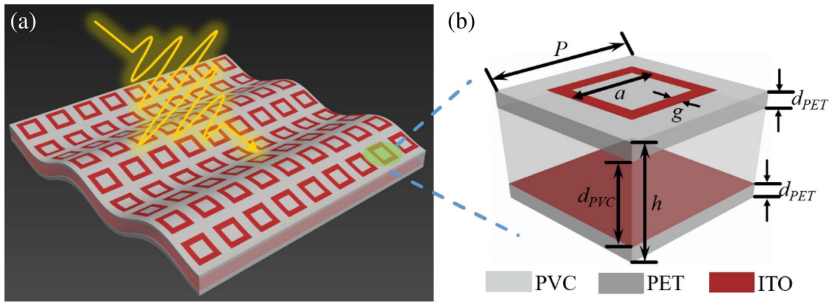

Fig. 1. (a) Schematic of the flexible and transparent MMA at millimeter frequencies. (b) Geometry of a unit cell.

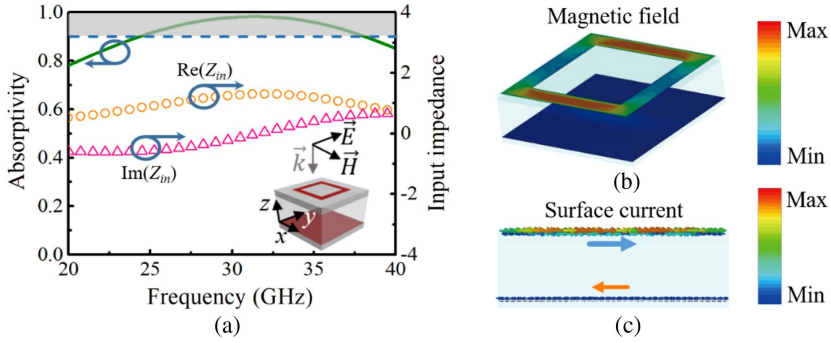

Fig. 2. (a) Simulated absorptivity spectra of the proposed MMA under normal incidence. (b), (c) Simulated magnetic field distribution and surface current distribution of the meta-atom at 32.0 GHz under normal incidence.

seen in Fig. 3(a), in which Z_0 and Z_d are the wave impedances of free space and the substrate, respectively. Z_S and $Y_S = 1/Z_S$ are the equivalent surface impedance and admittance of the top ITO pattern layer. From the TL theory [41], the reflection coefficient from the MMA can be calculated as

$$R = \frac{Z_{\text{in}} - Z_0^{\text{TE/TM}}}{Z_{\text{in}} + Z_0^{\text{TE/TM}}}, \tag{1}$$

where $Z_0^{\text{TE}} = Z_0/\cos\theta$ and $Z_0^{\text{TM}} = Z_0\cos\theta$ represent the wave impedances for TE and TM polarizations, respectively. θ is the incident angle. Z_{in} is the input impedance of the parallel circuit composed of Z_S and the grounded TL:

$$\frac{1}{Z_{\text{in}}} = \frac{1}{Z_S} + \frac{1}{jZ_d\tan\beta_r d}, \tag{2}$$

where β_r is the propagation constant of the substrate and d is the thickness of the substrate. It is clear that resonance occurs when

$$\beta_r d = \pi/2. \tag{3}$$

In this case, the grounded TL has infinite impedance, so that the reflection coefficient in Eq. (1) is only dependent on the matching degree between Z_S and Z_0. Under oblique incidence, the propagation constant within the substrate can be given by $\beta_r = k_0\sqrt{\varepsilon_r - \sin^2\theta}$, where $k_0 = 2\pi f_r/c$ is the free-space wavenumber. f_r is the resonance frequency, c is the speed of light, and ε_r is the relative permittivity of the substrate. From Eq. (3), the relationship between θ and f_r can be given by

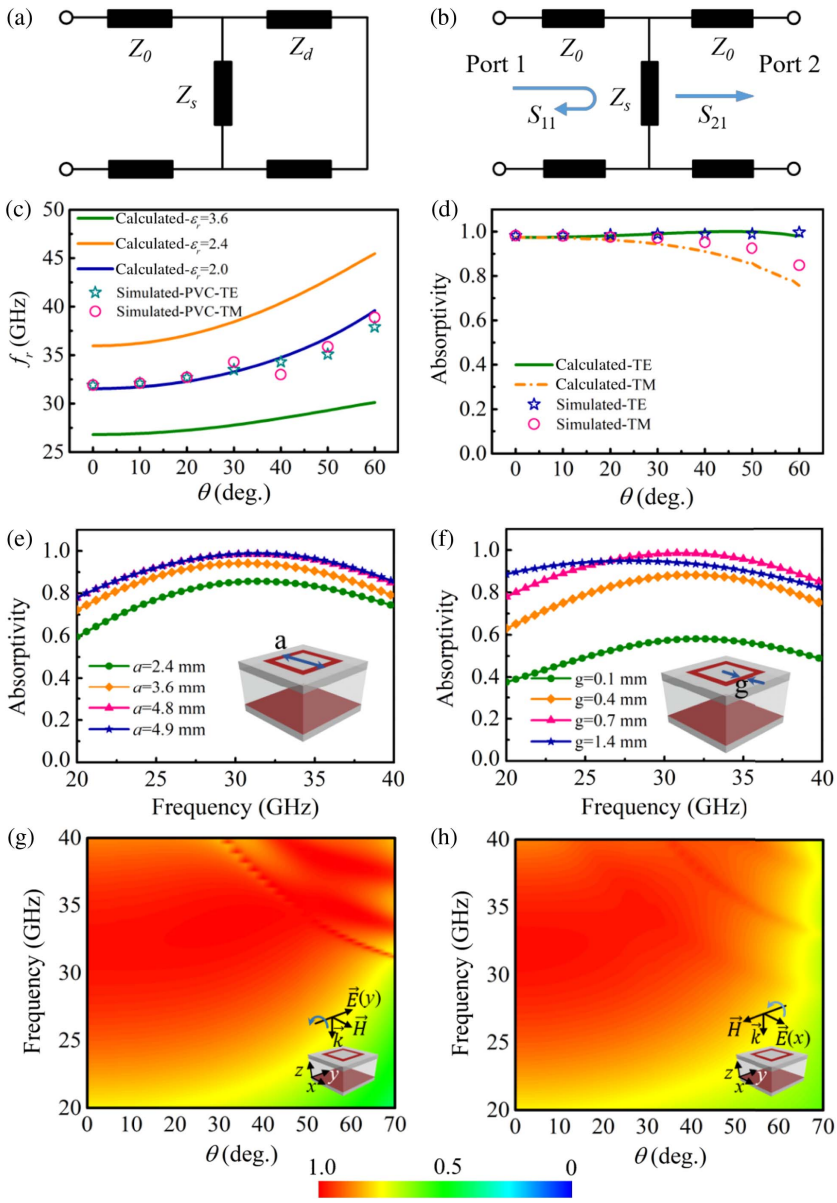

Fig. 3. (a) Schematic of the equivalent TL of the MMA. (b) TL model to retrieve the surface impedance of the ITO pattern. (c), (d) Calculated and simulated f_r as well as absorptivity with change of incident angle. (e), (f) Dependence of the simulated absorptivity spectra on side length a and line width g. (g), (h) Simulated absorptivity spectra of the proposed MMA at incident angles from 0° to 70° for TE and TM waves.

$$f_r = \frac{c}{4d\sqrt{\varepsilon_r - \sin^2\theta}}. \tag{4}$$

Since $Z_{\text{in}} = Z_S$ at the resonance frequency, the reflection coefficients for both polarizations in Eq. (1) can be further simplified as [42]

$$R^{\text{TE}} = \frac{Z_S \cos\theta - Z_0}{Z_S \cos\theta + Z_0}, \tag{5}$$

$$R^{\text{TM}} = \frac{Z_S - Z_0 \cos\theta}{Z_S + Z_0 \cos\theta}. \tag{6}$$

To determine the equivalent impedance of the ITO pattern layer, we can write the ABCD matrix of the ITO pattern layer as $\begin{bmatrix} 1 & 0 \\ 1/Z_S & 1 \end{bmatrix}$. For a typical two-port network, Z_S can be expressed as

$$Z_S = \frac{Z_0 S_{21}}{2 - 2S_{21}}, \tag{7}$$

where S_{21} is the forward transmission coefficient extracted from the TL model in Fig. 3(b), as can be simulated based on commercial electromagnetic solvers. From Eqs. (5)–(7), we can predict the location of the resonance frequency as well as the reflection coefficient of the meta-atom for dual polarizations, with respect to different incident angles and ITO patterns. Due to the small surface resistance of the ITO ground, it is reasonable to neglect the transmitted wave, and the absorption rate can be simplified as $A = 1 - |R|^2$.

When the thickness of the proposed MMA ($d_{\text{PET}} + d_{\text{PVC}}$) is close to $\lambda/4$ at 32.0 GHz, resonant frequency as a function of incident angle θ under TE and TM incidences is as demonstrated by stars and dots in Fig. 3(c), in which the theoretical values from Eq. (4) are also provided by way of contrast. Here, the polarization directions of the TE and TM waves are parallel to y- and x-directions, respectively [see Figs. 3(g) and 3(h)]. Accordance between the two results reveals that our model provides a good tool to predict a shift of the resonance peak with change of incident angle. Figure 3(c) also illustrates the dependence of the calculated resonance frequency on the substrate permittivity ε_r as θ grows up to 60°. Olive, orange, and blue lines represent the variance curves of f_r with $\varepsilon_r = 2.0$, 2.4, and 3.6, respectively. The resonance position f_r experiences a blue shift with increase of incident angle. Besides, it is worth noting that the initial value and the slope of the curve are highly associated with the permittivity of the substrate. Specifically, for a substrate with a low dielectric constant ($\varepsilon_r = 2.0$), the resonance frequency shifts to a high-frequency area rapidly at large θ; this affects the bandwidth of the MMA adversely. However, in the case of a substrate with large permittivity ($\varepsilon_r = 3.6$), the resonance frequency falls below 27.0 GHz at normal incidence, making it hard to operate within the target band effectively. It is therefore essential to choose ε_r properly when both the absorption bandwidth and frequency shift are taken into account. Fortunately, it seems that PVC with $\varepsilon_r = 2.4(1 - j0.06)$ is a good candidate to meet all these criteria, as found in Fig. 3(c).

To further verify the theoretical model, the absorptivity spectra of the MMA at f_r, as calculated from Eqs. (5)–(7), are provided in Fig. 3(d), with incident angle up to 60°. In the TE case, the simulated absorptivity (stars) coincides with the theoretical one (green line) very well. However, in the TM case, little discrepancy emerges at large angles, which is likely related to the induced high-order modes between the pattern and ground. Accuracy may improve if a multi-mode TL is employed [43]. In general, this model plays an important role in estimating the performance of the absorber in advance.

It is also important to adjust the element geometry for optimal absorption bandwidth and intensity. Two parameters, namely, the ring length a and the line width g in Fig. 1, are varied in Figs. 3(e) and 3(f) to observe the trend of absorptivity. Here g is fixed at 0.7 mm in Fig. 3(e) and a is fixed at 4.8 mm in Fig. 3(f). From the parameter scan analysis, a combination of $g = 0.7$ mm and $a = 4.8$ mm is eventually selected to achieve satisfactory absorption performance. The angular dependences of absorptivity for dual polarizations are illustrated in Figs. 3(g) and 3(h). Obviously the proposed MMA still offers excellent polarization-independent absorption rate from 25.5 to 40.0 GHz in a large angular range from 0° to 60°, and so it is feasible to use it as a conformal absorber in the millimeter band. Due to the existence of high-order resonant modes at large incident angles, some abrupt jumps in absorption rate for both TE and TM cases are observed at corresponding frequencies, although it has little effect on the whole absorption performance of the proposed MMA.

To confirm the absorption properties of the proposed MMA in the conformal case, full-wave simulations are performed when it is coated on a cylindrical metallic surface. Figures 4(a) and 4(b) show, respectively, the scenarios of TE and TM illumination toward the surface at the angles of $\theta = 90°$ and $\varphi = 0°$. The far-field scattering patterns on the xoz plane for the surface with the MMA coat are compared from Figs. 4(c) to 4(h) at 32.0 GHz, where different target radii of curvature of $r = 75$, 150, and 500 mm are considered with the same cylinder height of $H = 150$ mm. The scattering patterns of a same-size surface without coating are also provided in Fig. 4 for better observation of the scattering suppression. The directivity of the scattered beam improves significantly with increase of radius, as can be easily understood since a larger effective aperture size is achieved for wider cylinders. The conformal absorber is insensitive to the wave polarizations as we can tell in Figs. 4(c)–4(h); this can be ascribed to the symmetry of the meta-atom. Considerable RCS reductions are shown for the curved surfaces with the aid of the MMA for dual polarizations, with an average value of more than 10 dB when r is larger than 75 mm. The growth of the radius r leads to a decreased curvature of the surface. In consequence, a larger RCS reduction can be obtained for the conformal MMA coating when r grows to 150 and 500 mm, as shown in Figs. 4(i) and 4(j), respectively.

Note that the reflection from the conformal MMA is significantly suppressed in all directions at 32.0 GHz for TE [Figs. 4(c)–4(e)] and TM [Figs. 4(f)–4(h)] waves. Furthermore, RCS reduction of more than 7.5 dB (equal to absorptivity of 0.82) of the curved MMA is observed from 26.0 to 40.0 GHz for dual polarizations as r increases from 75 to 500 mm; this is consistent with the simulated absorptivity at oblique incidence in Figs. 3(g) and 3(h).

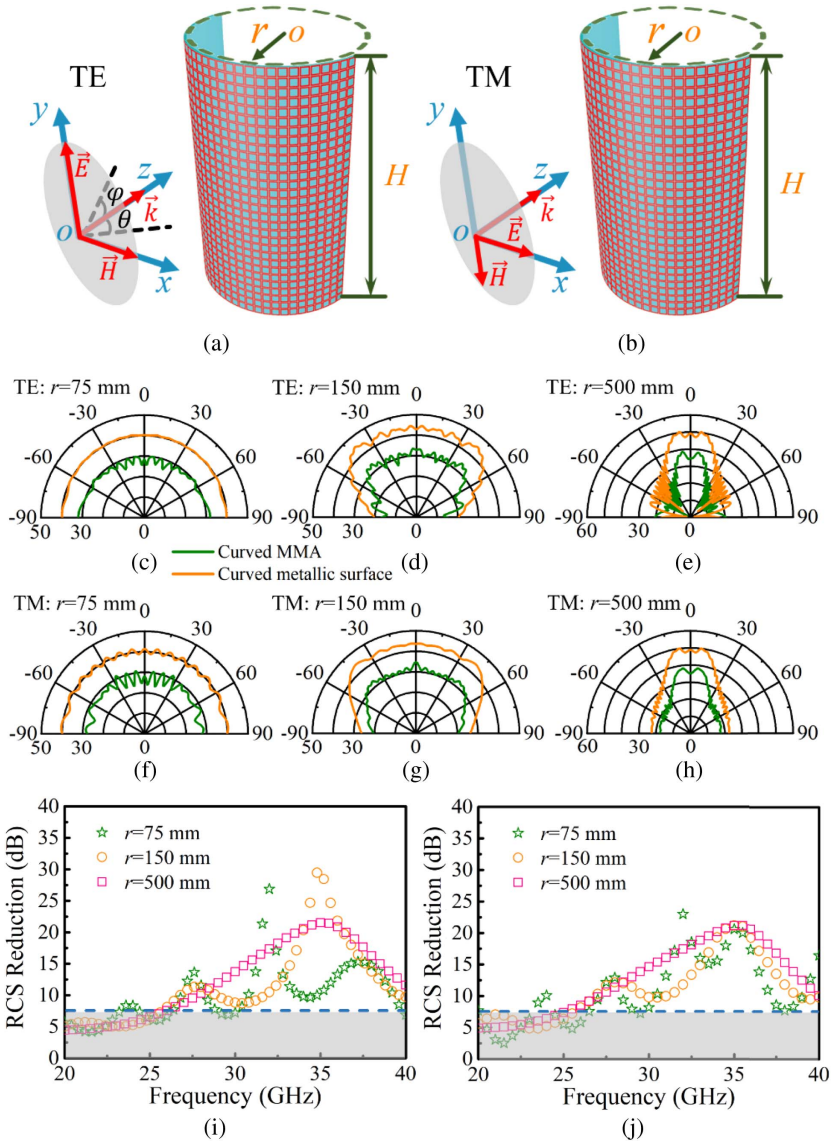

Fig. 4. (a), (b) Schematic of the conformal MMA backed by a conducting cylindrical surface under normal incidence of TE and TM waves. (c)–(h) Scattering patterns on the *xoz* plane at 32.0 GHz for TE and TM waves with $r = 75$, 150, and 500 mm. (i), (j) Simulated RCS reduction of the MMA coating compared with the control conducting surface of the same size for TE and TM waves with $r = 75$, 150, and 500 mm.

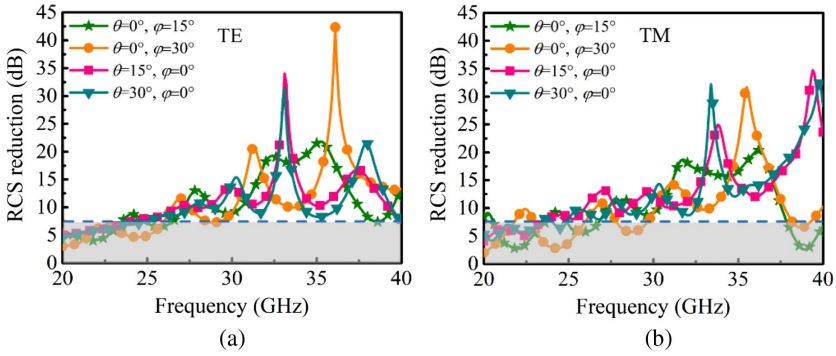

Fig. 5. Simulated angular stability of the MMA coating compared with the control conducting surface of the same size for (a) TE and (b) TM waves with $r = 75$ mm.

Finally, since the angular performance of the curved surface is also very important for practical applications, the simulated RCS reduction of the MMA-coated curved metal surface is presented in Figs. 5(a) and 5(b), where the radius of curvature $r = 75$ mm. Different incident angles and polarization states are taken into account from 20.0 to 40.0 GHz. Considerable RCS reduction from the MMA coating is achieved at oblique incidence within the frequency range of interest. However, the growth of the incident angle will highlight the problem of impedance mismatch, and therefore lead to worsened performance at some frequencies, as shown in Fig. 5.

3. FABRICATION AND MEASUREMENT

The fabricated sample is illustrated in Fig. 6(a). The periodic rings on the top ITO film are produced via laser etching, in which the processing accuracy is 10 μm. An ultrathin layer of optically clear adhesive is used for interlayer adhesion with excellent light transmittance performance. The sample has a size of 155 mm × 150 mm × 1.65 mm in total. The cylindrical surface is made of 304 stainless steel (electric conductivity 1.37×10^6 S/m and thickness 1.5 mm) using Computer Numerical Control Machine Tools (CNC).

The electromagnetic performance of the sample is characterized through the free-space method to measure the backward reflectivity as shown in Fig. 6(b). Swept sinusoidal signals from 20.0 to 40.0 GHz are transmitted and received through a pair of broadband antennas. A vector network analyzer (Agilent N5230C) is connected with the two antennas with phase-stable cables to determine the reflection and transmission coefficients from the sample. The sample is mounted on a platform opposite to the antennas as shown by a dashed line in Fig. 6(b). Since the transmitted energy is almost totally blocked by the ITO ground, the absorptivity can be written as $A = 1 - |S_{11}^2|$. Three rounds of measurement are performed in the experiment for calibration and normalization of reflectivity for the planar and curved MMAs; in these measurements, the sample, a control conducting plate, and a control conducting curved

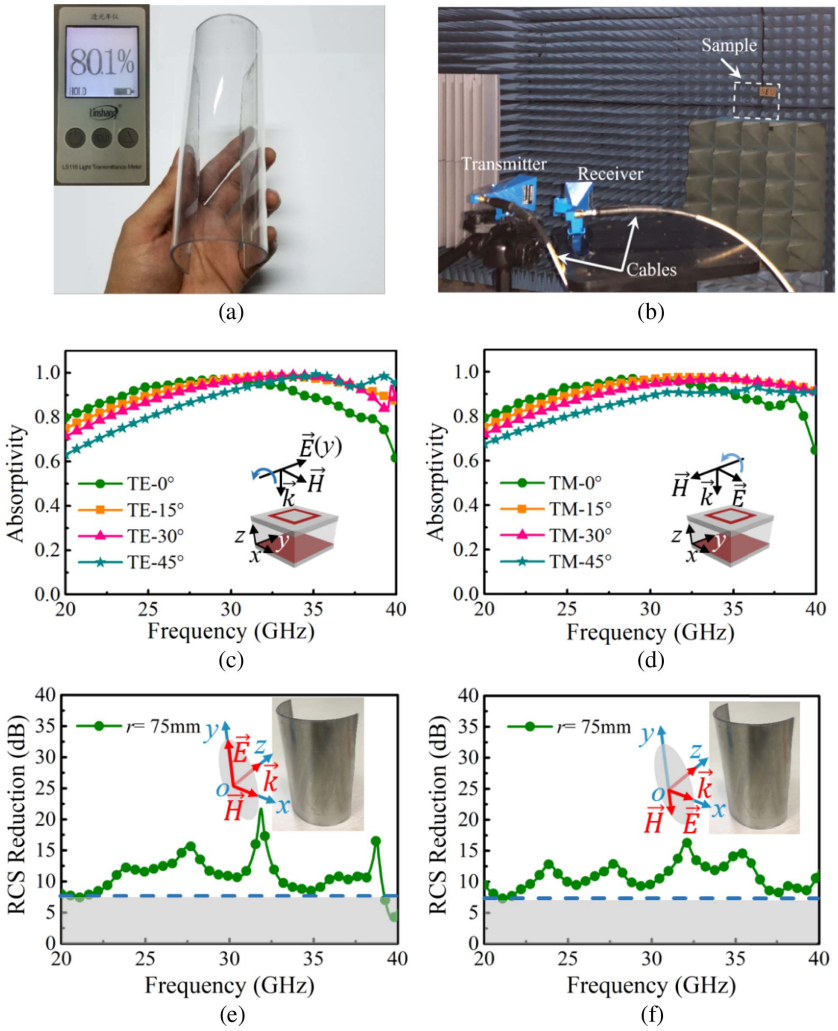

Fig. 6. (a) Photograph of the fabricated sample, where the inset shows the measured light transmittance. (b) The whole experimental setup in a microwave chamber. (c), (d) Measured absorptivity spectra of the proposed MMA from 20.0 to 40.0 GHz at angles of 0°, 15°, 30°, and 45° for TE and TM waves. (e), (f) Measured RCS reduction of the MMA coating compared with the control conducting surface of the same size with $r = 75$ mm under normal incidence of TE and TM waves.

surface are measured separately for comparison. Optical transmittance measurement is carried out with a light transmittance meter (LS116; Shenzhen Linshang Technology Co., Ltd) with accuracy smaller than ±1%.

4. RESULTS AND DISCUSSION

Figures 6(c) and 6(d) demonstrate the measured absorptivity of the planar MMA from 20.0 to 40.0 GHz. In accordance with the simulation predictions, the experimental results exhibit the advantages of polarization insensitivity, a wide bandwidth, and angular stability. Large absorptivity is obtained from 24.7 to 38.8 GHz, which is greater than 90% under normal incidence. The minor deviation between the simulated and measured absorption bandwidths is primarily due to the fabrication and assembly tolerances, measurement errors, and the variance of permittivity of the substrates. Absorptivity remains stable when the incident angle is below 45°, remaining above 80% in the whole Ka band. In addition, the measured light transmittance of the sample is about 80.1% in Fig. 6(a), making it suitable for window applications in practice. The measured backward RCS reduction of the MMA-coated curved surface ($r = 75$ mm) under normal incidence of TE and TM waves is plotted in Figs. 6(e) and 6(f), respectively. Although the measured RCS reduction traces are red-shifted, the experimental results [Figs. 6(e) and 6(f)] show good agreement with the simulated ones [Figs. 3(e) and 3(f), respectively], proving that the proposed absorber can indeed reduce backward reflection with high efficiency, and showing the potentials of the proposed MMA for conformal applications.

5. CONCLUSION

We have demonstrated designs and experimental characterizations of a conformal broadband MMA with good optical transparency. A ring-shaped unit cell is employed to achieve broadband absorption from 24.7 to 38.8 GHz, with measured optical transmittance of 80.1%, owing to the magnetic resonance driven by the incident waves. When coated on a curved cylindrical surface, the MMA still operates well from 25.5 to 40.0 GHz in a large angular range up to 60°. Moreover, by using soft substrates like PET and PVC, the proposed MM is made especially suitable for flexible absorbers in the microwave and for THz engineering.

Funding. National Key Research and Development Program of China (2017YFA0700201, 2017YFA0700202, 2017YFA0700203); National Natural Science Foundation of China (NSFC) (11227904, 61138001, 61371035, 61501112, 61501117, 61522106, 61571117, 61631007, 61701107, 61701108, 61722106, 61731010); 111 Project (111-2-05); Natural Science Foundation of Jiangsu Province (BK20150020); Fundamental Research Funds for the Central Universities (KYCX17_0091); Postgraduate Research & Practice Innovation Program of Jiangsu Province (KYCX17_0091); Scientific Research Foundation of Graduate School of Southeast University (YBJJ1812).

†These authors contributed equally to this work.

REFERENCES

1. Y. Naito and K. Suetake, "Application of ferrite to electromagnetic wave absorber and its characteristics," IEEE Trans. Microwave Theory Tech. **19**, 65–72 (1971).
2. S. Ohkoshi, S. Kuroki, S. Sakurai, K. Matsumoto, K. Sato, and S. Sasaki, "A millimeter-wave absorber based on gallium-substituted ε-iron oxide nanomagnets," Angew. Chem. Int. Ed. **46**, 8392–8395 (2007).
3. A. Namai, S. Kurahashi, H. Hachiya, K. Tomita, S. Sakurai, K. Matsumoto, Y. Goto, and S. Ohkoshi, "High magnetic permeability of ε-$Ga_xFe_{2-x}O_3$ magnets in the millimeter wave region," J. Appl. Phys. **107**, 09A955 (2010).
4. L. B. Kong, Z. W. Li, L. Liu, R. Huang, M. Abshinova, Z. H. Yang, C. B. Tang, P. K. Tan, C. R. Deng, and S. Matitsine, "Recent progress in some composite materials and structures for specific electromagnetic applications," Int. Mater. Rev. **58**, 203–259 (2013).
5. H. L. Lv, Y. H. Guo, Z. H. Yang, Y. Cheng, L. Y. P. Wang, B. S. Zhang, Y. Zhao, Z. C. J. Xu, and G. B. Ji, "A brief introduction to the fabrication and synthesis of graphene based composites for the realization of electromagnetic absorbing materials," J. Mater. Chem. C **5**, 491–512 (2017).
6. T. J. Cui, "Microwave metamaterials," Nat. Sci. Rev. **5**, 134–136 (2017).
7. T. J. Cui, "Microwave metamaterials—from passive to digital and programmable controls of electromagnetic waves," J. Opt. **19**, 084004 (2017).
8. D. R. Smith and J. B. Pendry, "Homogenization of metamaterials by field averaging," J. Opt. Soc. Am. B **23**, 391–403 (2006).
9. N. I. Landy, S. Sajuyigbe, J. J. Mock, D. R. Smith, and W. J. Padilla, "Perfect metamaterial absorber," Phys. Rev. Lett. **100**, 207402 (2008).
10. Q. Cheng, T. J. Cui, W. X. Jiang, and B. G. Cai, "An omnidirectional electromagnetic absorber made of metamaterials," New J. Phys. **12**, 063006 (2010).
11. C. M. Watts, X. Liu, and W. J. Padilla, "Metamaterial electromagnetic wave absorbers," Adv. Mater. **24**, OP98–OP120 (2012).
12. Z. H. Jiang, S. Yun, F. Toor, D. H. Werner, and T. S. Mayer, "Conformal dual-band near-perfectly absorbing mid-infrared metamaterial coating," ACS Nano **5**, 4641–4647 (2011).
13. R. Yahiaoui, J. P. Guillet, F. de Miollis, and P. Mounaix, "Ultra-flexible multiband terahertz metamaterial absorber for conformal geometry applications," Opt. Lett. **38**, 4988–4990 (2013).
14. H. Tao, C. M. Bingham, A. C. Strikwerda, D. Pilon, C. Shrekenhamer, N. I. Landy, K. Fan, X. Zhang, W. J. Padilla, and R. D. Averitt, "Highly flexible wide angle of incidence terahertz metamaterial absorber: design fabrication and characterization," Phys. Rev. B **78**, 241103 (2008).
15. K. Iwaszczuk, A. C. Strikwerda, K. Fan, X. Zhang, R. D. Averitt, and P. U. Jepsen, "Flexible metamaterial absorbers for stealth applications at terahertz frequencies," Opt. Express **20**, 635–643 (2012).
16. F. Zhang, S. Feng, K. Qiu, Z. Liu, Y. Fan, W. Zhang, Q. Zhao, and J. Zhou, "Mechanically stretchable and tunable metamaterial absorber," Appl. Phys. Lett. **106**, 091907 (2015).
17. Y. C. Fan, F. L. Zhang, Q. Zhao, Z. Y. Wei, and H. Q. Li, "Tunable terahertz coherent perfect absorption in a monolayer graphene," Opt. Lett. **39**, 6269–6272 (2014).
18. Y. Fan, Z. Liu, F. Zhang, Q. Zhao, Z. Wei, Q. Fu, J. Li, C. Gu, and H. Li, "Tunable mid-infrared coherent perfect absorption in a graphene meta-surface," Sci. Rep. **5**, 13956 (2015).
19. B. Wu, H. M. Tuncer, M. Naeem, B. Yang, M. T. Cole, W. I. Milne, and Y. Hao, "Experimental demonstration of a transparent graphene millimeter wave absorber with 28% fractional bandwidth at 140 GHz," Sci. Rep. **4**, 4130 (2014).
20. Y. Okano, S. Ogino, and K. Ishikawa, "Development of optically transparent ultrathin microwave absorber for ultrahigh-frequency RF identification system," IEEE Trans. Microw. Theory Tech. **60**, 2456–2464 (2012).
21. C. Zhang, Q. Cheng, J. Yang, J. Zhao, and T. J. Cui, "Broadband metamaterial for optical transparency and microwave absorption," Appl. Phys. Lett. **110**, 143511 (2017).

22. J. Zhao, C. Zhang, Q. Cheng, J. Yang, and T. J. Cui, "An optically transparent metasurface for broadband microwave antireflection," Appl. Phys. Lett. **112**, 073504 (2018).
23. D. W. Hu, J. Cao, W. Li, C. Zhang, T. L. Wu, Q. F. Li, Z. H. Chen, Y. L. Wang, and J. G. Guan, "Optically transparent broadband microwave absorption metamaterial by standing-up closed-ring resonators," Adv. Opt. Mater. **5**, 1700109 (2017).
24. T. Jang, H. Youn, Y. J. Shin, and L. J. Guo, "Transparent and flexible polarization-independent microwave broadband absorber," ACS Photon. **1**, 279–284 (2014).
25. Y. Shen, J. Q. Zhang, L. H. Shen, S. Sui, Y. Q. Pang, J. F. Wang, H. Ma, and S. B. Qu, "Transparent and broadband absorption-diffusion-integrated low-scattering metamaterial by standing-up lattice," Opt. Express **26**, 28363–28375 (2018).
26. Y. Shen, J. Q. Zhang, L. H. Shen, S. Sui, Y. Q. Pang, J. F. Wang, H. Ma, and S. B. Qu, "Transparent absorption-diffusion-integrated water-based all-dielectric metasurface for broadband backward scattering reduction," J. Phys. D **51**, 485301 (2018).
27. Y. Shen, J. Q. Zhang, Y. Q. Pang, J. F. Wang, H. Ma, and S. B. Qu, "Transparent broadband metamaterial absorber enhanced by water–substrate incorporation," Opt. Express **26**, 15665–15674 (2018).
28. J. Sun, L. Liu, G. Dong, and J. Zhou, "An extremely broad band metamaterial absorber based on destructive interference," Opt. Express **19**, 21155–21162 (2011).
29. Y. Shen, J. Q. Zhang, Y. Y. Meng, Z. L. Wang, Y. Q. Pang, J. F. Wang, H. Ma, and S. B. Qu, "Merging absorption bands of plasmonic structures via dispersion engineering," Appl. Phys. Lett. **112**, 254103 (2018).
30. S. Liu, H. Chen, and T. J. Cui, "A broadband terahertz absorber using multi-layer stacked bars," Appl. Phys. Lett. **106**, 151601 (2015).
31. B. Monacelli, J. B. Pryor, B. A. Munk, D. Kotter, and G. D. Boreman, "Infrared frequency selective surface based on circuit-analog square loop design," IEEE Trans. Anntenas Propag. **53**, 745–752 (2005).
32. D. S. Dong, J. Yang, Q. Cheng, J. Zhao, L. H. Gao, S. J. Ma, S. Liu, H. B. Chen, Q. He, W. W. Liu, Z. Fang, L. Zhou, and T. J. Cui, "Terahertz broadband low-reflection metasurface by controlling phase distributions," Adv. Opt. Mater. **3**, 1405–1410 (2015).
33. D. Y. Shchegolkov, A. K. Azad, J. F. O'Hara, and E. I. Simakov, "Perfect subwavelength fishnetlike metamaterial-based film terahertz absorbers," Phys. Rev. B **82**, 205117 (2010).
34. P. K. Singh, K. A. Korolev, M. N. Afsar, and S. Sonkusale, "Single and dual band 77/95/110 GHz metamaterial absorbers on flexible polyimide substrate," Appl. Phys. Lett. **99**, 264101 (2011).
35. X. P. Shen, Y. Yang, Y. Zang, J. Gu, J. Han, W. Zhang, and T. J. Cui, "Triple-band terahertz metamaterial absorber: design, experiment, and physical interpretation," Appl. Phys. Lett. **101**, 154102 (2012).
36. H. Tao, N. I. Landy, C. M. Bingham, X. Zhang, R. D. Averitt, and W. J. Padilla, "A metamaterial absorber for the terahertz regime: design, fabrication and characterization," Opt. Express **16**, 7181–7188 (2008).
37. F. Ding, Y. Cui, X. Ge, Y. Jin, and S. He, "Ultra-broadband microwave metamaterial absorber," Appl. Phys. Lett. **100**, 103506 (2012).
38. J. Zhu, Z. Ma, W. Sun, F. Ding, Q. He, L. Zhou, and Y. Ma, "Ultra-broadband terahertz metamaterial absorber," Appl. Phys. Lett. **105**, 021102 (2014).
39. X. Chen, B.-I. Wu, J. A. Kong, and T. M. Grzegorczyk, "Retrieval of the effective constitutive parameters of bianisotropic metamaterials," Phys. Rev. E **71**, 046610 (2005).
40. X. Chen, T. M. Grzegorczyk, B. I. Wu, J. Pacheco, and J. A. Kong, "Robust method to retrieve the constitutive effective parameters of metamaterials," Phys. Rev. E **70**, 016608 (2004).
41. D. M. Pozar, *Microwave Engineering*, 2nd ed. (Wiley, 1998).
42. B. A. Munk, P. Munk, and J. Pryor, "On designing Jaumann and circuit analog absorbers (CA absorbers) for oblique angle of incidence," IEEE Trans. Antennas Propag. **55**, 186–193 (2007).
43. S. Maci, M. Caiazzo, A. Cucini, and M. Casaletti, "A pole-zero matching method for EBG surfaces composed of a dipole FSS printed on a grounded dielectric slab," IEEE Trans. Antennas Propag. **53**, 70–81 (2005).